OPEN ACCESS

ACTA METALLURGICA SLOVACA

2026, VOL. 32, NO. 3, 220-227

RESEARCH PAPER

The insights into the phase transformation kinetics of middle-carbon Mn-Si high-strength steels: Effect of manganese content

Vasily Efremenko[1,2], Yuliia Chabak[1,2], Ivan Petrišinec[1], Alexey Efremenko[2], Maria Podobova[1], Mikhailo Brykov[3,4]

[1]Institute of Materials Research of Slovak Academy of Science, Str. Watsonova 47, 04001 Košice, Slovakia
[2]Pryazovskyi State Technical University, Str. Gogolya 29, 49044 Dnipro, Ukraine
[3]Technische Universität Berlin, 10623 Berlin, Germany
[4]National University Zaporizhzhia Polytechnic, 69011 Zaporizhzhia, Ukraine

*Corresponding author: viefremenko@saske.sk, vgefremenko@gmail.com, tel.: 421-950234614, Division of Metallic Systems, Institute of Materials Research of Slovak Academy of Science, 04001, Košice, Slovakia

Received: 05.08.2026
Accepted: 24.08.2026

ABSTRACT

This study investigates the influence of manganese additions ranging from 2.6 to 8.2 wt.% on the transformation behavior of undercooled austenite in 0.5 wt.% C – (1.6-2.8) wt.% Si steels. Experimental results reveal a systematic decrease in critical transformation temperatures Ac_1 and Ac_3 with increasing Mn, which is accompanied by a shift in transformation mechanisms. At lower Mn levels (2.6-3.1 wt.%), heating induces a two-stage transformation characterized by abnormal expansion and the separation of pearlitic and ferritic reactions, whereas higher Mn contents (6.3-8.2 wt.%) promote a continuous transformation with diminished volumetric and thermal effects. Dilatometric cooling experiments demonstrate that the critical cooling rate (V) required to fully suppress pearlite/bainite formation is $0.1 < V \leq 0.5$ °C/s for the Mn2.6 and Mn3.1 steels, and is bounded by an upper threshold of $V \leq 0.1$ °C/s for the Mn6.3 and Mn8.2 grades, giving way to a martensitic transformation. Consecutively, the Ms temperatures decrease from 218 °C to below 50 °C as Mn increases from 2.6 to 8.2 wt.%. Finite-difference thermal simulations show that diffusional decomposition of undercooled austenite is suppressed during air cooling of plates up to 20 mm in the Mn2.6-3.1 steels and up to 50 mm in the Mn6.3-8.2 steels. Thermodynamic modeling highlights the pronounced retardation of bainitic transformation with increasing Mn, culminating in near-complete suppression at 8.2 wt.%. Finally, pre-quenching below M_s significantly accelerates the subsequent bainitic transformation by reducing incubation times and enhancing transformation rates, as demonstrated for the 2.6 wt.% Mn steel grade.

Keywords: high-strength steels, manganese, phase transformations, critical temperatures, dilatometry

INTRODUCTION

The progress of high-strength and ultra-high-strength steels, especially for automotive and structural applications, depends on the development of Advanced High-Strength Steels (AHSS) of the third generation. The main challenge in metallurgy is to combine high tensile strength with sufficient ductility and impact toughness [1]. To achieve this, modern heat treatment methods such as austempering [2, 3] and Quenching and Partitioning (Q&P) [4, 5] are widely used. These processes create complex microstructures consisting of martensite, bainite, and a controlled fraction of carbon-enriched retained austenite (RA). Retained austenite plays a decisive role in this balance, as it enhances ductility and strength through the Transformation-Induced Plasticity (TRIP) effect, first described by Zackay et al. and later refined by Olson and Cohen [1, 6]. More recent studies, such as those by Rykavets et al. [7] and Harjukelo et al. [8], have demonstrated that the stability of retained austenite in TRIP-assisted steels can be tuned through alloying and heat-treatment strategies.

Silicon is a key element in the above heat treatments, as it suppresses cementite precipitation during bainitic transformation and partitioning stage, ensuring that carbon remains in the austenite matrix. This effect was highlighted in the work of Bhadeshia [9] and later confirmed by Garcia-Mateo et al. [10]. Manganese is another important alloying element for the third generation AHSSs [11]. It lowers the martensite start temperature, retards ferrite and pearlite formation, and stabilizes overcooled austenite [12]. 3rd-generation middle-Mn steels demonstrate superior global formability compared with conventional 1st-generation AHSSs [13]. Recent works [14, 15] have shown that steels with 3-8 wt.% Mn and ~2-2.5 wt.% Si can achieve through-thickness hardening of bulk steel products under air cooling.

Traditionally, austempering and Q&P require strict control of thermodynamic and kinetic parameters during cooling. Medium-carbon steels treated this way are usually quenched rapidly into molten salt baths, hot oil, or fluidized beds to suppress pearlite and ferrite formation [16]. While effective in laboratory conditions, molten bath quenching is difficult to scale up. Salt baths pose environmental hazards, increase operational costs, and demand complex maintenance procedures. They also introduce safety risks associated with handling and disposal of high-temperature chemicals. Furthermore, rapid liquid quenching often generates high residual stresses, leading to distortion, warping, or microcracking in components with complex geometries [17, 18]. Thus, the need for alternative cooling strategies that are safer and more economical has appeared [19, 20].

Air cooling has been proposed as a simpler and safer route [21, 22]. It eliminates the necessity of using an expensive quenching media, reduces logistical complexity, and ensures a more uniform thermal gradient across treated parts. However, achieving fully martensitic, bainitic, or multiphase structures through relatively slow air cooling requires profound modifications of steel chemistry. The alloy must exhibit high hardenability so that the critical cooling rate is low enough to prevent diffusional decomposition of austenite during exposure to air. Medium-carbon steels heavily alloyed with silicon and manganese are promising candidates [23]. By varying manganese content up to 10-12 wt.%, the overall hardenability of the medium-carbon matrix can be shifted to unprecedented levels [24]. However, under higher manganese content, incubation periods for bainite formation become significantly prolonged, which can affect the uniformity of the final microstructure [25]. Also, high manganese additions introduce complexities. Severe microsegregation [26] and banding may occur, leading to chemical inhomogeneity [27]. Moreover, Wang et al. [28] showed that Mn segregation at phase boundaries during hot deformation further slows interphase migration, adding another layer of complexity to industrial processing.

Although the general thermodynamic effects of manganese on steel hardenability are well documented, the specific kinetic nuances (critical temperatures and cooling rates), shifts in transformation pathways, and structural parameters in 0.5%C-2.5%Si systems with high manganese concentrations remain insufficiently clarified [29]. From a practical engineering perspective, there is a lack of predictive data linking manganese content directly to the maximum section thickness (critical diameter) that can undergo through-hardening under ambient air cooling. This lack in knowledge limits the ability of engineers to design reliable industrial heat treatment regimes for medium-Mn steels.

To address this gap, the present study investigates the transformation kinetics of 0.5C–2.5Si–(3-8)Mn steels. Using high-resolution dilatometry, differential scanning calorimetry, microstructural analysis, and thermodynamic simulation, the transformation behaviors under heating and cooling were mapped. The goal is to clarify the role of manganese in delaying diffusional transformations and determine the maximum plate or bar thickness that can be uniformly hardened during simplified air-cooling treatments.

MATERIAL AND METHODS

The experimental steels were initially produced using a 50 kg induction furnace and cast into 50-mm diameter sand molds. To ensure chemical and structural homogeneity, the resulting cast billets underwent electroslag remelting, yielding cylindrical ingots with a diameter of 90 mm. The chemical compositions of the fabricated alloys are detailed in **Table 1**. These ingots were subsequently forged and hot-rolled to produce strips with a final thickness of 12 mm. To relieve residual stresses and establish a baseline state, the rolled strips were annealed at 850 °C, followed by controlled slow cooling that included an isothermal holding step at 550 °C for 2 h, with subsequent cooling to room temperature inside the switched-off furnace. Test specimens for both microstructural characterization and mechanical evaluations were extracted from the annealed strips using wire electrical discharge machining.

To determine the critical phase transformation temperatures (Ac_1, Ac_3, and M_s), quenching dilatometric analyses were carried out using a Linseis L78 RITA dilatometer on cylindrical specimens (4 mm in diameter, 10 mm in length) machined from the annealed material. The experimental procedure, calibration, and data acquisition were conducted in strict accordance with the ASTM A1033 standard practice for high-speed dilatometry of steels. The tangent method was applied to the resulting linear thermal expansion curves to identify the critical transformation points. During the dilatometric cycles, the specimens were heated under a protective inert atmosphere at a constant rate of 5 ºC/s to an austenitization temperature of 900 ºC, held isothermally for 300 s, and subsequently cooled to room temperature at rates of 0.1, 0.5, 1.0, and 10.0 ºC/s. To evaluate the effect of the pre-quenching treatment, specific samples were rapidly cooled at 50 °C/s to target temperatures below Ms, immediately followed by reheating to 300 °C for subsequent isothermal partitioning. Following the dilatometric runs, metallographic examination was conducted to verify the microstructural constituents.

The thermal analysis of phase transformations during heating was conducted via Differential Scanning Calorimetry (DSC) using a Netzsch Jupiter STA449 F1 DTA/DSC/TG thermal analyzer. The DSC runs were performed at a constant heating rate of 10 K/min under controlled conditions, utilising an empty Al_2O_3 crucible as a reference. The characteristic transition temperatures were determined using the integrated Proteus Thermal Analysis (version 5.2.0) software. Additionally, thermodynamic equilibrium calculations and phase simulations were carried out using the JMatPro® software package.

To ensure the statistical reproducibility of the experimental results, three independent specimens were tested for each thermal cycle condition during both the quenching dilatometric and DSC runs. The parallel measurements exhibited high consistency, with the critical transformation temperatures deviating by less than ±5 °C, and the representative thermal curves were graphically presented in the manuscript.

Specimens for microstructural analysis were prepared using standard metallographic procedures according to ASTM E3 guidelines, followed by chemical etching using a 4% Nital solution in compliance with ASTM E407. The microstructure was characterized using an optical microscope (OM) Olympus GX71 and a scanning electron microscope (SEM) JEOL JSM-7000F.

Table 1 Chemical composition (wt.%) of the experimental steels

Steel	C	Si	Mn	Cr	Ni	V	Nb	S	P
Mn2.6	0.45	1.57	2.61	0.09	0.09	–	–	0.010	0.010
Mn3.1	0.54	2.85	3.06	0.10	0.07	–	0.01	0.016	0.021
Mn6.3	0.52	2.19	6.32	0.10	0.09	0.08	0.04	0.013	0.023
Mn8.2	0.50	2.83	8.19	0.10	0.07	0.11	0.04	0.008	0.020

RESULTS AND DISCUSSION

Microstructure of annealed steels

Fig. 1 presents the microstructure of the investigated steels in the annealed state. The steels with low manganese content (Mn2.6 and Mn3.1) exhibited a visually identical microstructure entirely consisting of pearlite (**Figs. 1a and 1c**), represented by eutectoid $\alpha Fe+M_3C$ colonies of varying dispersion (**Fig. 1b**). In the steel with a higher manganese content (6.3 wt.%), the microstructure became more complex: along with fine pearlite colonies, extensive areas of bainite with an acicular morphology occupied most of the sample area (**Figs. 1d and 1e**). The light-contrast zones distributed across the bainitic needles presumably correspond to residual austenite or a co-existing mixture of retained austenite and freshly formed martensite. In the steel with the highest manganese content (Mn8.2), the microstructure primarily consists of retained austenite matrix with pearlite along the grain boundaries (pearlite colony pattern is shown in the inset of **Fig. 1f**). From these pearlite areas, occasional martensite or bainite needles are observed protruding into the austenite grains. The presence of austenite is evidenced by slip bands resulting from the deformation of the γ-phase during metallographic sample preparation. These data demonstrate that as the manganese content increases to 6.3-8.2 wt.%, retained austenite appears in the as-annealed structure, reflecting the γ-stabilizing role of manganese. The slow cooling conditions during the annealing process were insufficient to ensure the complete transformation of the Mn-rich austenite via a diffusional mechanism.

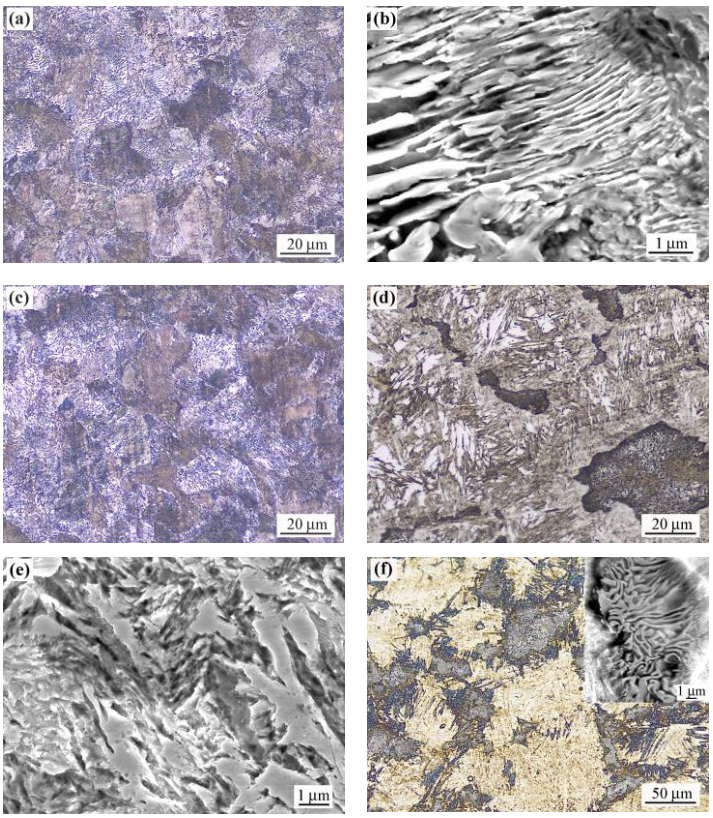

Fig. 1 Microstructure of the steels in the annealed state: (a, b) Mn2.6; (c) Mn3.1; (d, e) Mn6.3; (f) Mn8.2 (a, c, d – OM; b, e – SEM; f – OM/SEM)

Critical points measurements

The experimental dilatograms in **Fig. 2** and the quantified critical temperatures (Ac_1 and Ac_3) in **Table 2** demonstrate a clear multi-stage nature of austenitization in alloyed steels with elevated Mn and Si contents, as well as a competitive thermodynamic interplay between the ferrite-stabilizing effect of silicon and the austenite-stabilizing effect of manganese. According to the heating curves presented in **Fig. 2a**, the slope of the curve within the region preceding the Ac_1 point increases with higher manganese content. This behavior is attributed to a progressive accumulation of retained austenite within the microstructure, which has a higher coefficient of thermal expansion as compared to the αFe phase.

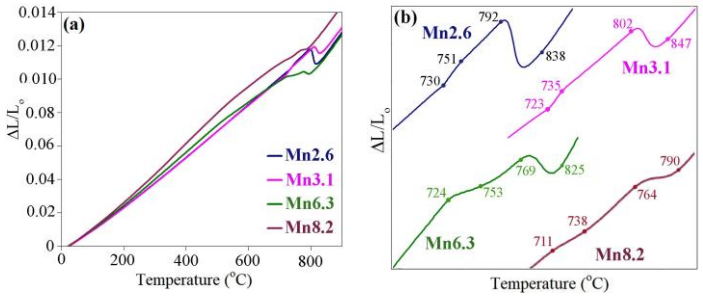

Fig. 2 Dilatometric heating curves of studied steels with different manganese contents: (a) relative length change ($\Delta L/L_0$) as a function of temperature during continuous heating. (b) magnified view of the α→γ phase transformation zone

Table 2 The critical temperatures (°C) of the studied steels

Steel	Ac_1	Ac_3	M_s	Critical cooling rate, V (°C/s)
Mn2.6	730	838	218	0.1<V≤0.5
Mn3.1	723	847	196	0.1<V≤0.5
Mn6.3	724	825	92	V≤0.1
Mn8.2	711	790	< 50	V≤0.1

Note: The critical cooling rate defines the threshold required to fully suppress non-martensitic (diffusional) transformations during cooling.

The detailed heating profiles reveal the sequence of phase transformations during heating as a function of local manganese concentration. For the low-manganese steels (containing 2.6 wt.% and 3.1 wt.% Mn), a distinct upward inflection in the linear expansion rate is observed in the range of 730-751 °C for Mn2.6 and 723-735 °C for Mn3.1. This section is followed by a flatter region, after which a sharp decrease in the specimen length is recorded starting from 792 °C for Mn2.6 and 802 °C for Mn3.1. The first stage represents the abnormal expansion region described in [30]. The appearance of this region is attributed to the presence of a certain amount of retained austenite (RA) in the initial microstructure and the initiation of cementite carbide dissolution. Carbon enriches the retained austenite, leading to an increase in the specific volume of the γ-phase. Since the transformation at this stage does not generate new portions of austenite, the heating curve records an expansion region rather than the contraction typical of the αFe→γFe transformation [31, 32]. As the transformation progresses, the contraction begins to dominate over the thermal expansion of austenite. Consequently, the abnormal expansion region is first replaced by a section with a lower slope (e.g., 751-792 °C for Mn2.6) and subsequently by a region of sharp length reduction corresponding to the intensive development of the transformation. According to the authors of [31], the onset of the abnormal expansion region represents the true Ac_1 point, whereas using the distinct inflection on the dilatogram (e.g., 792 °C for Mn2.6) yields significantly overestimated values for this critical point. The presence of the abnormal expansion region indicates the existence of RA in the initial microstructure of the Mn2.6 and Mn3.1 steels, despite the absence of visible signs of its presence (**Figs. 1a and 1b**).

In contrast to these steels, no abnormal expansion region is observed in the steels with a higher manganese content (Mn6.3 and Mn8.2). Immediately after the onset of the transformation (Ac_1 = 724 °C for Mn6.3 and 711 °C for Mn8.2), a decrease in the curve slope occurs. Manganese strongly stabilizes austenite and lowers the Ac_1 temperature. At high manganese contents, the transformation initiates at a lower temperature where carbon diffusion is still sufficiently rapid. Manganese promotes the rapid formation of a large number of austenite nuclei. Therefore, the transformation proceeds intensively immediately after the Ac_1 point, meaning that the volumetric contraction (αFe→γFe) begins to dominate from the very beginning, without a noticeable «enrichment stage» of the existing austenite. Starting from a specific temperature (753 °C for Mn6.3 and 738 °C for Mn8.2), the slope of the curve temporarily increases; this can be attributed to the thermal expansion of the accumulated austenite starting to override the phase contraction. This section is replaced by a section of length reduction in the Mn6.3 steel or a plateau in the Mn8.2 steel, corresponding to the maximum transformation rate. Noteworthy is the absence of specimen contraction in the steel with the maximum manganese content, which is explained by the large amount of austenite in the microstructure of the annealed steel and the lowest αFe→γFe volume decrease. For this steel, the transformation was completed at the lowest temperature among all steels (790 °C), reflecting the γ-stabilizing effect of manganese.

To independently validate the thermodynamic and kinetic mechanisms deduced from the dilatometric analysis, differential scanning calorimetry was performed during continuous heating up to 1200 °C. The experimental DSC curves for the low-manganese (2.6 wt.% Mn) and high-manganese (8.2 wt.% Mn) steels are comparatively displayed in **Fig. 3**. The calorimetric thermal effects correlate with the critical temperatures identified by dilatometry.

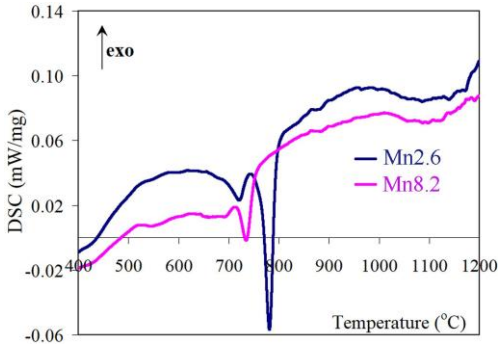

Fig. 3 DSC heating curves of steel Mn2.6 and Mn8.2

The presented DSC heating curve clearly demonstrates the significant difference in behavior between the steels with low (Mn2.6) and high (Mn8.2) manganese contents. More specifically: the Mn2.6 steel is characterized by a distinct and deep endothermic peak with a minimum at 782 °C, which corresponds to the intensive phase transformation. This is consistent with the dilatometry data, where sharp contraction is recorded immediately after 792 °C. In the Mn8.2 steel, the endothermic peak is substantially lower in intensity and shifted toward lower temperatures. This confirms that at high Mn content, the transformation initiates earlier, proceeds more gradually, and covers a wider temperature interval. Another distinctive feature is the two-stage austenitization process in the Mn2.6 steel, which exhibits a second (less intensive) endothermic peak starting from approximately 680 °C with a minimum at 725 °C. This peak can be associated with the pearlite-to-austenite transformation, which proceeds relatively fast. The second, deeper peak results from the transformation of proeutectoid (free) ferrite into austenite, which requires long-range carbon diffusion and occurs at higher temperatures [33]. A similar two-stage transformation behavior in low-alloy hypoeutectoid steels was previously recorded and described in [31, 32]. At low manganese content (2.6 wt.%), the two transformation stages are well-separated by temperature. At high manganese content (8.2 wt.%), the acceleration of austenite nucleation and the lowering of critical temperatures cause both stages to overlap; as a result, the transformation proceeds more continuously without a pronounced separation into “pearlitic” and “ferritic” parts.

The smooth, broad endothermic downward trend starting from 950 °C for the 2.61% Mn steel and shifting toward 1000 °C for the 8.2% Mn steel corresponds to the high-temperature dissolution of persistent carbides and the subsequent diffusion-driven chemical homogenization of the austenite solid solution. Due to the high nominal concentration of manganese in the 8.2% Mn steel, the carbide phases possess greater thermodynamic stability, and the substitution diffusion of Mn within the FCC lattice is significantly retarded. Consequently, this homogenization process requires higher thermal activation, shifting the onset of the heat consumption to 1000 °C.

To quantify the combined effects of silicon and manganese on the critical temperatures of the investigated steels, empirical regression equations were derived from the experimental dilatometric data:

Ac_1 (ºC) = 746.7 – 6.6·[%Si] – 1.8·[%Mn] (R^2=0.91) (1.)
Ac_3 (ºC) = 862.0 + 3.7·[%Si] – 9.1·[%Mn] (R^2=0.86) (2.)
where: [%Mn] and [%Si] – contents of manganese and silicon in steel, respectively.

Equation (2) demonstrates a classical thermodynamic behavior for the Ac_3 temperature, which marks the completion of the αFe→γFe transformation. In this stage, Mn acts as a strong austenite stabilizer, effectively lowering the Ac_3 point (with a coefficient of –9.1), whereas Si exhibits its well-known ferrite-stabilizing nature, raising the temperature required for full austenitization (with a coefficient of +3.7). In contrast, equation (1) reveals a seemingly paradoxical negative coefficient for silicon (–6.6) for the Ac_1 temperature. This behavior is driven by the low solubility of silicon in cementite and its ability to increase the thermodynamic activity of carbon in ferrite. Consequently, higher silicon levels destabilize the carbide phase, accelerating its dissolution and lowering the energy barrier for the transformation onset during heating. Furthermore, silicon stabilizes a certain fraction of retained austenite in the initial microstructure. During heating, this austenite acts as a preferential site for early carbon enrichment from dissolving carbides, triggering the abnormal expansion stage at lower temperatures. Since the onset of this abnormal expansion marks the true Ac_1 point, higher silicon contents shift the deviation from linear expansion downward. Therefore, while silicon acts as a macro-thermodynamic ferrite stabilizer at the final stage of austenitization (Ac_3), its impact on carbon activity and retained austenite stability dominates the initial stage, decreasing the Ac_1 temperature.

Continuous cooling transformations

The continuous cooling dilatometric curves presented in **Fig. 4** illustrate the transformation behavior of the 900 ºC-austenized steels down to room temperature, which highlight the stabilizing of austenite by manganese adding.

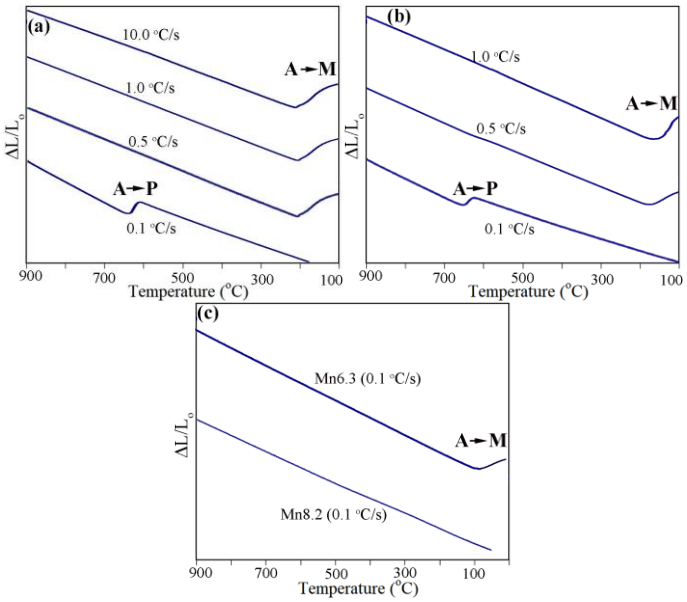

Fig. 4 Dilatometric cooling curves of steels: (a) Mn2.6, (b) Mn3.1, and (c) Mn6.3 and Mn8.2

For the steels with lower manganese concentrations, Mn2.6 (Fig.e 4a) and Mn3.1 (**Fig. 4b**), experiments were conducted across a wide range of cooling rates from 0.1 ºC/s to 10.0 ºC/s to identify the critical cooling rate for full martensitic hardening. At the slowest cooling rate of 0.1 ºC/s, both steels undergo a high-temperature diffusional transition which is manifested by a distinct upward deviation in the dilatometric curves, corresponding to the austenite-to-pearlite transformation. For the Mn2.6 steel, pearlitic transformation occurs in the temperature interval of 660-595 ºC. For the Mn3.1 steel, the increased manganese content shifts this transformation to slightly lower temperatures of 645-580 ºC range. The extensive diffusion time available at 0.1 ºC/s allows carbon and alloying elements to redistribute, preventing the retention of unstable austenite to lower temperatures. Increasing the cooling rate to higher values (0.5-10.0 ºC/s) suppressed the diffusional transformation in both steels while the expansion step shifted below 250 ºC, signifying the initiation of the athermal martensitic transformation. The dilatometric curves follow a perfectly linear thermal contraction pathway from 900 ºC down to approximately 218 ºC for Mn2.6 steel and 196 ºC for Mn3.2 steel (**Table 2**). This confirms that 0.5 ºC/s exceeds the critical cooling rate for these low-manganese grades, successfully freezing the austenite until it transforms entirely via the shear-dominant martensitic mechanism.

For the medium- and high-manganese steels, Mn6.3 and Mn8.2 (**Fig. 4c**), the cooling study was restricted to a single ultra-slow cooling rate of 0.1 ºC/s. This choice was dictated by the exceptionally high stability of undercooled austenite caused by elevated manganese contents which reduces the thermodynamic driving force for diffusional decomposition and retards the diffusion rates of carbon and substitutional atoms. The cooling curve for the Mn6.3 steel at a rate of 0.1 ºC/s exhibits a monotonic linear contraction down to approximately 92 ºC, where a distinct expansion onset marks the initiation of the martensitic transformation (A→M). This behavior demonstrates that the critical cooling rate required to suppress diffusional decomposition and successfully induce martensite formation in the Mn6.3 steel is extremely low, being no higher than of 0.1 ºC/s. It should be emphasized that these measurements were not aimed at precisely identifying the absolute critical cooling rate for the Mn6.3 and Mn8.2 steels, but rather at experimentally establishing its upper bound, which is carefully designated as ≤0.1 ºC/s. In the case of the Mn8.2 steel, the continuous cooling dilatogram at 0.1 ºC/s remains perfectly linear throughout the entire temperature spectrum down to 50 ºC with no expansion anomalies representing either diffusional or martensitic transformations are detected. This behavior demonstrates that an 8.2% Mn addition stabilizes the FCC austenite matrix to such an extent that the Ms temperature is depressed below, or the transformation kinetics are fully sluggish, resulting in a fully stable retained austenitic structure at ambient conditions, with its critical cooling rate safely remaining within the same ≤0.1 ºC/s boundary.

The dilatometric analysis results are well-supported by the microstructural investigation of the dilatometric specimens (**Fig. 5**).

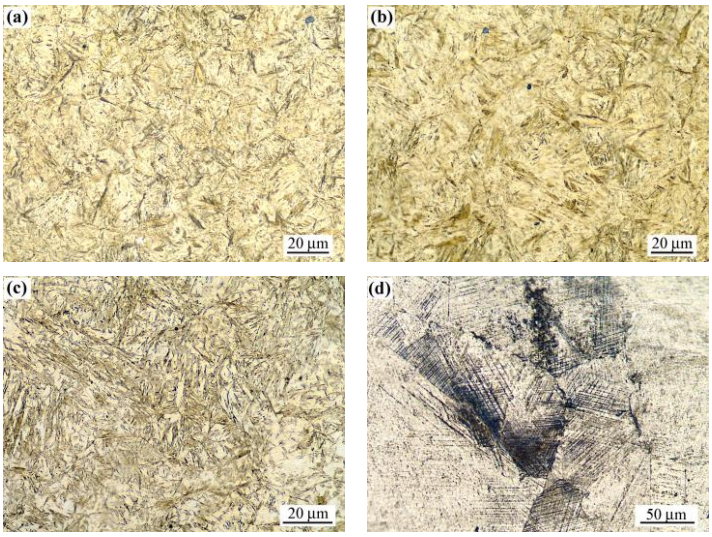

Fig. 5 Microstructure of the dilatometric samples after continuous cooling to room temperature: (a) Mn2.6 (1.0 ºC/s); (b) Mn3.1 (1.0 ºC/s); (c) Mn6.3 (0.1 ºC/s); (d) Mn8.2 (0.1 ºC/s) (a-d – OM)

As shown in **Figs. 5a and 5b**, cooling at a rate of 1.0 ºC/s leads to the formation of acicular martensite in the Mn2.6 and Mn3.1 steels, with no diffusional

transformation products (ferrite, pearlite, or bainite) detected in the microstructure. In the Mn6.3 steel, martensite is also present; however, the needle morphology becomes less pronounced, and the emergence of a bright background indicates an increased volume fraction of retained austenite, which is attributed to the twofold increase in manganese content (**Fig. 5c**). In contrast, no martensite is formed in the Mn8.2 steel due to the declining of the M_s temperature down to ambient room temperature. The resulting microstructure consists almost entirely of austenite grains with characteristic slip bands induced during metallographic sample preparation (**Fig. 5g**). Thus, the microstructure of the steels correlates well with the position of the martensite start temperature determined by the dilatometric method.

Air-cooling behavior of the steels

The critical cooling rates of the experimental steels provide a basis for evaluating their processability during heat treatments such as austempering and Q&P. These techniques require deep undercooling to low temperatures (within the bainitic and martensitic transformation ranges) while suppressing austenite decomposition in the high-temperature diffusion region. To achieve this, conventional routes employ liquid media (such as molten salts or liquid metals) that ensure the required cooling rates. However, the use of specialized quenching baths significantly complicates the manufacturing process. Therefore, implementing air cooling is highly desirable, which in turn demands enhanced hardenability of the steel. In this regard, it was of interest to evaluate the feasibility of utilizing the investigated steels under air-cooled austempering and Q&P conditions. For this purpose, the air-cooling rates of specific steel products – in this case, plates with thicknesses ranging from 5 to 50 mm – were determined and compared with the dilatometric cooling curves. Here, the cooling dynamics at the core of the product were of primary interest to ensure a homogeneous microstructure across the entire cross-section.
To predict the temperature distribution and cooling curves, a non-steady-state Fourier heat conduction equation was solved numerically in a one-dimensional formulation for an infinite plate (sheet) of thickness $2H$ [34]:

$$\rho \cdot c(T) \cdot \frac{\partial T}{\partial \tau} = \frac{\partial}{\partial x}\left(\lambda(T) \cdot \frac{\partial T}{\partial x} \right) \quad (3.)$$

where: T [°C] - temperature
τ [s] - time
x [m] - the coordinate along the sheet thickness ($-H \le x \le H$)
ρ [kg/m^3] - the steel density
c [J/(kg·K)] - the specific heat capacity
λ [W/(m·K)] - the thermal conductivity.

The initial and boundary conditions were defined as follows:
(a) uniform initial temperature distribution across the cross-section: $T(x, 0) = T_0 =$ 900 °C.
(b) symmetry condition at the centerline of the sheet (axial zone):

$$\left.\frac{\partial T}{\partial x}\right|_{x=0} = 0 \quad (4.)$$

(c) boundary condition of the third kind (Newton-Richmann convective heat transfer) at the cooled surfaces ($x = \pm H$):

$$-\lambda(T) \cdot \left.\frac{\partial T}{\partial x}\right|_{x=\pm H} = \alpha \cdot (T_{surf} - T_{air}) \quad (5.)$$

where: α [W/(m^2·K)] - the effective heat transfer coefficient (for still air α = 35 W/(m^2·K))

The governing equation was discretized using an implicitly formulated finite difference method, ensuring absolute numerical stability. The system coefficients are determined by the temperature-dependent variables c_i and λ_i updated at each time step using tabulated thermodynamic data exported from JMatPro® software. The calculations were performed for two steels, Mn2.6 and Mn8.2, which exhibit the maximum difference in manganese content and, consequently, in thermal conductivity (23-28 W/(m K) and 20-25 W/(m K), respectively). This variation governs the evolution of the temperature profile across the plate cross-section.
Fig. 6 presents the calculated cooling kinetics within the centerline of the steel plate during symmetric double-sided air cooling. The simulated cooling curves for the Mn2.6 (**Fig. 6a**) and Mn8.2 (**Fig. 6b**) steel grades demonstrate a strong non-linear dependence of the heat dissipation rate on the section thickness from 5 mm to 50 mm. For both alloys, the thermal profiles exhibit an exponential decay, where increasing the sheet thickness severely delays the temperature drop. The time required to cool the centerline below 200 °C increases from approximately 600 s for the thinnest 5 mm sheet to over 4000 s for the 50 mm section. A minor divergence is observed between the cooling curves of the two steel grades at identical thicknesses due to variation in thermophysical properties, induced by difference manganese concentrations. On the cooling rate curves in the thickness range of 15-20 mm, a distinct plateau is observed, representing a transitional stabilization in the heat transfer regime as it shifts from external convective air cooling to being limited by the internal thermal resistance of the steel plate. Within this critical range, surface heat loss and internal heat dissipation temporarily equilibrates, flattening the cooling rate.

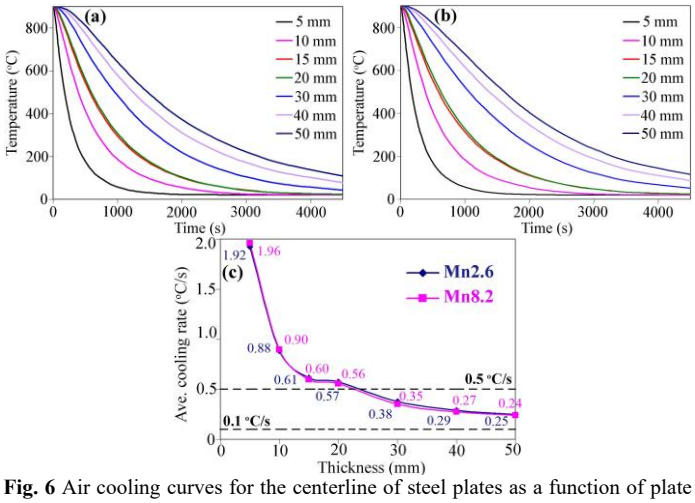

Fig. 6 Air cooling curves for the centerline of steel plates as a function of plate thickness for steels (a) Mn2.6 and (b) Mn8.2, and (c) variation in the average cooling rate of the steel sheet centerline across different plate thickness

The quantitative evolution of the average cooling rate (**Fig. 6c**) reveals that kinetic profiles for both steels follow a highly similar yet distinctly separated trend: the thinnest plates exhibit maximum cooling rates of 1.92 °C/s for Mn2.6 and 1.96 °C/s for Mn8.2, which drastically drop below 1.0 °C/s as the thickness reaches 10 mm. Within the critical thickness range of 15 to 25 mm, the cooling rate stabilizes near a key threshold, yielding 0.57 °C/s for Mn2.6 and 0.60 °C/s for Mn8.2 at a thickness of 20 mm. Beyond 30 mm, the heat transfer kinetics slow down, asymptotically approaching a minimum baseline of 0.25 °C/s and 0.24 °C/s for the 50 mm sheet, respectively. Comparison of the cooling-rate values in **Fig. 6c** with the dilatometric results (**Fig. 4**) shows that the Mn2.6 and Mn3.1 steels can be air-cooled in plate sections up to 20 mm without proeutectoid ferrite or pearlite formation, eliminating the need for liquid quenching media. Moreover, in the Mn6.3 and Mn8.2 steels, diffusional decomposition of undercooled austenite is completely suppressed during air cooling of plates with section thicknesses up to 50 mm. More specifically, in the Mn8.2 steel, due to the very low position of the Ms temperature, the steel retains a fully austenitic structure upon cooling to room temperature. This behavior is essential for processing routes that require preservation of overcooled austenite for subsequent low-temperature treatments.

Transformation kinetic at isothermal conditions

The effect of manganese on the kinetics of phase transformations under isothermal conditions was investigated using computer simulations with JMatPro® software. The simulation results are presented in **Fig. 7** as the combined time-temperature-transformation (TTT) and continuous cooling transformation (CCT) diagrams for the investigated steels. The thermodynamic

calculations reveal a profound impact of manganese content on both the incubation periods and the stabilization of undercooled austenite, significantly modifying the proeutectoid ferrite, pearlite, and bainite transformation fields.

For the lower manganese compositions (2.6-3.1 wt.%) variants (**Figs. 7a and 7b**), the diagrams exhibit three distinct transformation regions: proeutectoid ferrite, pearlite, and bainite. In the Mn2.6 steel, the isothermal curves for pearlite and bainite transformations are positioned at relatively short holding times, near 10 s at 600 ºC. Increasing the manganese content to 3.1 wt.% (**Fig. 7b**) induces a noticeable shift of bainite transformation noses toward longer times (300 s), with lowering the nose from 400 ºC to 370 ºC, demonstrating the moderate austenite-stabilizing effect of manganese in this concentration range.

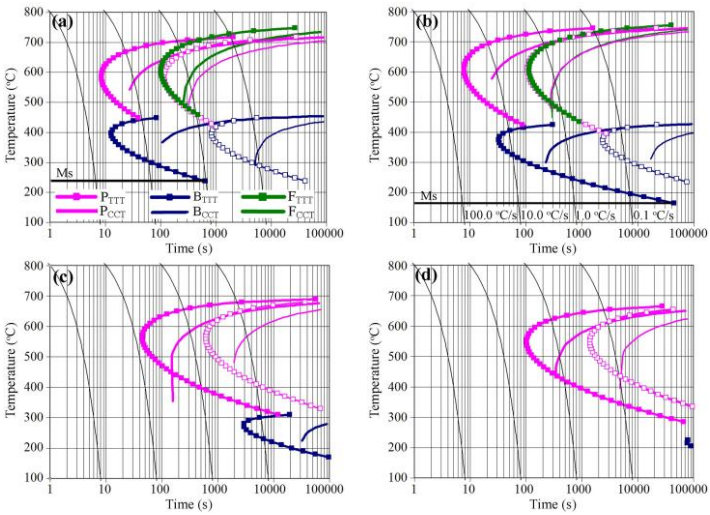

Fig. 7 Combined TTT and CCT diagrams of austenite transformation in the investigated steels (a) Mn2.6, (b) Mn3.1, (c) Mn6.3, (d) Mn8.2. The curve designations for the different transformation types are presented in Fig. 6a (P, B and F – pearlite, bainite and proeutectoid ferrite formation, respectively). The curves with solid and open symbols correspond to the formation of 0.1% and 99.9% of the phase, respectively

A dramatic alteration in the transformation kinetics is observed when the manganese content is doubled to 6.3 wt.% (**Fig. 7c**), completely suppressing the proeutectoid ferrite formation within the modeled timeframe. Furthermore, the pearlite transformation nose is heavily depressed in temperature (down to approximately 550 ºC) and significantly delayed, with the incubation period reaching 40 s, reflecting a substantial decrease in the critical cooling rate required to achieve a fully martensitic matrix. The bainite transformation region is similarly shifted toward longer times (3,000 s) with a nose decreased to ~275 ºC. At the highest manganese concentration of 8.2 wt.% (**Fig. 7d**), the trend toward stabilization of undercooled γ-phase reaches its peak. The pearlite transformation field is restricted and shifted to ~100 s, while the bainite transformation curve is almost completely suppressed, initiating only after prolonged holding times.

The effects of manganese on the incubation period of pearlite and bainite transformations under isothermal conditions are summarized in **Fig. 8**, confirming that manganese acts as a potent solute retardant for both diffusional and intermediate austenite decomposition, with the magnitude of delay being strongly sensitive to the specific transformation temperature. This pronounced retardation is governed by the thermodynamic and kinetic effects of manganese as a substitution alloying element. Manganese decreases the chemical driving force for γ→α transformation and a cementite nucleation and lowers the diffusivity of carbon in austenite [36]. Additionally, in medium-manganese steels, Mn segregation is observed at phase boundaries, which further retards interface migration and dissipates energy [28]. The retarding effect of manganese on the transformation kinetics is more pronounced in the bainitic region: in Mn8.2 steel, the intermediate transformation is virtually locked; the incubation point can only be modeled at an extremely depressed temperature of 225 ºC, where it requires nearly 100,000 s to initiate. Thus, high manganese additions stabilize the undercooled austenite lattice to such an extent that the cooperative, shear-driven nucleation mechanism of bainitic ferrite laths is kinetically frozen, facilitating the retention of an austenitic-martensitic state upon cooling [37]. This finding indicates that austempering or other heat treatments involving the austenite-to-bainite transformation are not feasible for the Mn6.3 and Mn8.2 steels. In contrast, for the Mn2.6 and Mn3.1 steels, the bainitic transformation, which is typically realized at temperatures of 250-300 ºC, is completed within a reasonable holding time according to the simulation: within 1.5-2.5 h (at 300 ºC) and 7.5-10 h at 250 ºC.

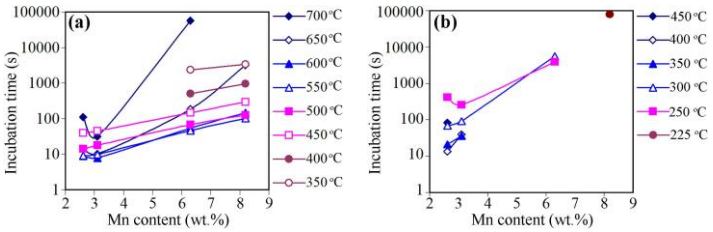

Fig. 8 Influence of manganese content on the incubation period of (a) pearlite and (b) bainite transformations at different isothermal holding temperatures

Given that the stability of austenite in the bainitic transformation region increases sharply with higher manganese content, the possibility of accelerating the bainitic reaction through the partial austenite-to-martensite transformation was investigated. As reported in [38], the appearance of martensite significantly accelerates subsequent bainite development due to an increased dislocation density, the generation of new phase boundaries that facilitate bainite nucleation, and the creation of localized fields of high elastic strain. To confirm this hypothesis regarding the studied steels, the steel Mn2.6 was subjected to austempering at 300 ºC while the isothermal holding was preceded by rapid cooling (with a rate of 50 ºC/s) to 195 ºC, 175 ºC, and 145 ºC, which are below the M_s temperature of this steel (218 ºC, **Table 2**). According to **Fig. 3**, cooling at this rate prevents pearlite and bainite transformations, which is a prerequisite for the austempering treatment. After cooling, the samples were immediately heated to 300 ºC. This heat treatment cycle was performed using the dilatometer. The volume fraction of martensite (f_m) formed during the pre-cooling stage was estimated using the Koistinen-Marburger relationship [39]:

$$f_m\,(\text{vol.}\%) = 1 - \exp(-a_m \cdot (Ms - T_Q)) \qquad (6.)$$

where: T_Q [ºC] – quenching temperature
a_m – fitting coefficient (0.012)
M_s [ºC] – martensite start temperature.

The volume fractions of martensite were calculated as 24%, 40%, and 58% for pre-quenching to 195 ºC, 175 ºC, and 145 ºC, respectively. The dilatometric curves presenting the length changes of the pre-quenched specimens during isothermal holding at 300 ºC are showing in **Fig. 9a** (the plotted sections originate from the exact moment the holding temperature was reached).

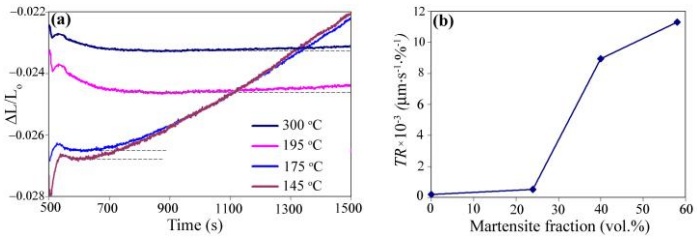

Fig. 9 (a) Dilatometric curves of the bainitic transformation at 300 ºC in the Mn2.6 steel pre-quenched to 195 ºC, 175 ºC, and 145 ºC. (b) Effect of martensite volume fraction on the *I* parameter value

The initial cooling-heating cycle accompanied by sharp length alterations, were succeeded by a stabilization stage (a plateau) observed on all curves. After a certain holding period, the curves begin to deviate upward from the horizontal

baseline, signaling the onset of the γFe→αFe transformation, which proceeds with a volumetric expansion. Using the curve slope, parameter "Transformation Rate *(TR)*" was calculated to evaluate the rate of a bainite reaction at early stage of transformation. As the volumetric effect of phase transition depends on the austenite amount, the *TR* accounts for the fraction of austenite remaining after pre-quenching, as follows:

$$TR = \frac{\Delta L}{\Delta \tau} \cdot \frac{1}{(1 - f_m)}, \quad (7.)$$

where: ΔL [μm] - the specimen length change
$\Delta \tau$ [s^{-1}] – holding duration
f_m [vol.%] – martensite volume fraction found by Eq. (6.).

In the non-pre-quenched specimen, the transformation required approximately 1050 s to start after the specimen reached 300 ºC, representing the incubation period for this temperature (**Fig. 9a**). At the initial stage, the transformation proceeds rather slowly ($TR = 0.2 \cdot 10^{-3}$ μm/(s·%), **Fig. 9b**). Pre-quenching to 195 ºC, which generated 24% martensite, moderately reduced the incubation period to ~960 s and slightly accelerated bainite transformation ($TR = 0.5 \cdot 10^{-3}$ μm/(s·%)). The introduction of 40 vol.% martensite drastically catalyzed the transformation, as evidenced by an almost twofold reduction in the incubation period (to 675 s) and a sharp increase in the curve slope (to $TR = 8.9 \cdot 10^{-3}$ μm/(s·%)). Increasing the martensite fraction to 58% (at T_Q=145 ºC) further reduced the incubation period to 643 s; however, it had lower additional impact on the transformation rate, yielding a slope close to that of the T_Q = 175 ºC and *TR* of 11.3 μm/(s·%). A comparison of the results for different T_Q temperatures demonstrates that pre-quenching indeed accelerates the bainitic transformation of austenite in Mn2.6 steel. However, there is a specific range for the martensite fraction where this effect is most pronounced. For the investigated steel, this optimal window is close to 40 vol.%; a lower martensite content fails to induce a strong accelerating effect, while a higher content leads to a saturation of its influence.

A comparison of the experimental and calculated data regarding the transformation kinetics in the investigated steels allows for assessing the accuracy of the thermodynamic simulation. As follows from **Fig. 9**, the transformation in the Mn2.6 steel at 300 ºC initiates after approximately 1050 s, whereas the simulation results show an incubation period of only 72 s at this temperature. Furthermore, according to the CCT diagrams, the critical cooling rate for martensite formation is about 10.0 ºC/s for the Mn2.6 and Mn3.1 steels, is within the range of 1.0-10.0 ºC/s for the Mn6.3 steel, and is approximately 1.0 ºC/s for the Mn8.2 steel. Comparing these data with the obtained experimental results (Table 2) indicates that the simulation significantly underestimates the stability of undercooled austenite in the investigated steels. This discrepancy must be taken into account when selecting heat treatment regimes for medium-manganese steels, and the thermodynamic simulation results should be experimentally verified [40].

CONCLUSIONS

In this work, the effect of manganese within the range of 2.6-8.2 wt.% on the features and kinetics of undercooled austenite phase transformation in 0.5 wt.% C – (1.6-2.8) wt.% Si steels was investigated, and the following conclusions were drawn:

1. A clear trend of decreasing critical temperatures Ac_1 and Ac_3 with increasing manganese content has been observed: Ac_1 dropped from 730 ºC to 711 ºC, and Ac_3 from 838 ºC to 790 ºC. For the 2.6-3.1 wt.% Mn steels, the transformation during heating occurs via a two-stage mechanism, characterized by the appearance of an abnormal expansion region on the dilatogram and the separation of pearlitic and ferritic transformations on the DSC curve. As the Mn content increases to 6.3-8.2 wt.%, the transformation proceeds continuously without stage separation, exhibiting less pronounced volumetric and thermal effects. Empirical regression equations describing the effects of Mn and Si on the Ac_1 and Ac_3 points in the investigated steels have been established.
2. In the 2.6 and 3.1 wt.% Mn steels, cooling at 0.1 ºC/s induces the pearlite transformation, whereas rates of 0.5-10.0 ºC/s suppress diffusional decomposition, leading to martensite formation (M_s = 218 ºC and 196 ºC, respectively). In the 6.3 and 8.2 wt.% Mn steels, pearlite and bainite reactions are fully suppressed even at 0.1 ºC/s, while M_s drops to 92 ºC (Mn6.3) and to room temperature (Mn8.2). Thermal simulation indicates that the hardenability of the Mn2.6 and Mn3.1 grades is sufficient for through-thickness air hardening of plates up to 20 mm thick without using a liquid media. Meanwhile, in the Mn6.3 and Mn8.2 steels, diffusional decomposition of overcooled austenite is completely suppressed during air cooling of plates with section thicknesses up to 50 mm.
3. Thermodynamic simulation established that increasing manganese significantly prolongs incubation periods and lowers transformation "nose" temperatures under isothermal conditions. Crucially, the bainitic transformation undergoes a more pronounced retardation: the bainite "nose" shifts from 10 s at 400 ºC (Mn2.6) to 300 s at 370 ºC (Mn3.1) and further to 3000 s at 275 ºC (Mn6.3). For the Mn8.2 steel, this transformation is virtually blocked, requiring holding times exceeding 100,000 s at 225 ºC.
4. Pre-quenching the 2.6 wt.% Mn steel below M_s significantly reduces the incubation period and accelerates the subsequent bainitic transformation at 300 ºC. The acceleration onset occurs with a 24% martensite fraction formed at 195 ºC. At 40% martensite (cooling to 175 ºC), the incubation period is halved (from 1050 to 675 s) and the initial bainite growth rate increases sharply. At a 58% martensite fraction (cooling to 145 ºC) this accelerating effect reaches saturation.

Acknowledgements: This research is funded by the Slovak Research and Development Agency (project number APVV-23-0341).

REFERENCES

1. S. Bai et al.: Journal of Materials Research and Technology, 27, 2023, 2216–2236. https://doi.org/10.1016/j.jmrt.2023.09.210
2. H. Zheng et al.: Crystals, 15(12), 2025, 1044. https://doi.org/10.3390/cryst15121044
3. H. Jirková, K. Opatova, Š. Jenicek, J. Vrtacek, L. Kučerová, P. Kurka: Acta Metallurgica Slovaca, 25(2), 2019, 101–106. https://doi.org/10.12776/ams.v25i2.1267
4. V.G. Efremenko et al.: Materials Today Communications, 47, 2025, 113179. https://doi.org/10.1016/j.mtcomm.2025.113179
5. J. Escherova et al.: Metals, 16(4), 2026, 362. https://doi.org/10.3390/met16040362
6. W. Bleck, X. Guo, Y. Ma: Steel Research International, 88(12), 2017, 1700218. https://doi.org/10.1002/srin.201700218
7. Z.M. Rykavets et al.: Uspehi Fiziki Metallov, 20(4), 2019, 620–633. https://doi.org/10.15407/ufm.20.04.620
8. V. Harjukelo, O. Nousiainen, P. Kantanen, J. Kömi, S. Pallaspuro: Materials Characterization, 235, 2026, 116341. https://doi.org/10.1016/j.matchar.2026.116341
9. H.K.D.H. Bhadeshia: *Bainite in Steels: Theory and Practice*, 3rd ed., London: Institute of Materials, Minerals and Mining, Maney Publishing, 2015
10. R. Rana, E. Cordova-Tapia, L. Morales-Rivas, J.A. Jimenez, C. Garcia-Mateo: Materials Science and Engineering A, 931, 2025, 148236. https://doi.org/10.1016/j.msea.2025.148236
11. M. Franceschi, J.A. Jimenez, C. Garcia-Mateo, R. Rana: Steel Research International, 2026, e202501219. https://doi.org/10.1002/srin.202501219
12. I. Apurwa, J.K. Yadav, A. Kumar: Lecture Notes in Mechanical Engineering, 2023. https://doi.org/10.1007/978-981-19-1618-2_34
13. A. Payà, M. Carpio, D. Frómeta: Solid State Phenomena, 388, 2026, 163-170. https://doi.org/10.4028/p-pkv0mr
14. M.K. Singh, A. Kumar Verma, A. Kumar: Materials Today: Proceedings, 56(1), 2022, 356–367. https://doi.org/10.1016/j.matpr.2022.01.195
15. A. Tjahjono, F.G. Pramesti, N.S. Frendyta, P.A. Paristiawan: Jurnal Ilmu Fisika Universitas Andalas, 16(1), 2024, 79–87. https://doi.org/10.25077/jif.16.1.79-87.2024
16. M. Sedlaček, G. Klančnik, A. Nagode, J. Burja: Materials, 14, 2021, 7518. https://doi.org/10.3390/ma14247518
17. V.I. Zurnadzhy et al.: Metallurgical and Materials Transactions A, 51, 2020, 3042–3053. https://doi.org/10.1007/s11661-020-05737-w
18. A. Samuel, K.N. Prabhu: Journal of Materials Engineering and Performance, 31, 2022, 5161–5188. https://doi.org/10.1007/s11665-022-06667-x
19. V. Zurnadzhy et al.: Materials, 17, 2024, 1958. https://doi.org/10.3390/ma17091958
20. X. Fang et al.: Metals, 16, 2026, 65. https://doi.org/10.3390/met16010065

21. S,G. Lee, M. Kaviany, J. Lee: International Journal of Heat and Mass Transfer, 189, 2022, 122702. https://doi.org/10.1016/j.ijheatmasstransfer.2022.122702
22. S. Ahmed, O. Oja, A. Kaijalainen, P. Peura: steel research international, 96, 2025, 2400420. https://doi.org/10.1002/srin.202400420
23. A.D. Koval' et al.: Journal of Friction and Wear, 33(2), 2012, 153–159. https://doi.org/10.3103/S1068366612020079
24. E. De Moor, J. Speer, D. Matlock, J. Kwak, S.-B. Lee: ISIJ International, 51(1), 2011, 137–144. https://doi.org/10.2355/isijinternational.51.137
25. M. Morawiec, J. Opara, C. Garcia-Mateo, J. Jiménez, A. Grajcar: Journal of Thermal Analysis and Calorimetry, 148, 2022, 1567–1576. https://doi.org/10.1007/s10973-022-11664-2
26. B. Trembach et al.: Eng, 6, 2025, 125. https://doi.org/10.3390/eng6060125
27. V. Efremenko et al.: Crystals, 16, 2026, 325. https://doi.org/10.3390/cryst16050325
28. W. Wang, Y. Liang, L. Wang, H. Xu, P. Lyu: Materials Characterization, 234, 2026, 116230. https://doi.org/10.1016/j.matchar.2026.116230
29. X. Wang, K. Spitzer: Steel Research International, 93, 2022, 2200173. https://doi.org/10.1002/srin.202200173
30. W.L. Bevilaqua et al.: Metallurgical and Materials Transactions A, 54, 2023, 3349–3357. https://doi.org/10.1007/s11661-023-07105-w
31. D. San Martín, T. Cock, A. García-Junceda, F. Caballero, C. Capdevila, C.G. de Andrés: Materials Science and Technology, 24(3), 2008, 266–272. https://doi.org/10.1179/174328408X265640
32. J. Rezaei, M. Habibi Parsa, H. Mirzadeh: Journal of Materials Research and Technology, 27, 2023, 2524–2537. https://doi.org/10.1016/j.jmrt.2023.10.089
33. V. Efremenko et al.: Acta Metallurgica Slovaca, 26(3), 2020, 116–121. https://doi.org/10.36547/ams.26.3.554
34. F. Incropera, D. DeWitt, T. Bergman, A. Lavine: *Fundamentals of Heat and Mass Transfer*, John Wiley & Sons, 2007.
35. O.H. Kurpe, V.V. Kukhar, E.S. Klimov, S.M. Chernenko: Materials Science Forum, 989, 2020, 609-614. https://doi.org/10.4028/www.scientific.net/MSF.989.609
36. G. Stornelli et al.: Acta Metallurgica Slovaca, 28(3), 2022, 127–132. https://doi.org/10.36547/ams.28.3.1535
37. M. Morawiec, A. Grajcar, W. Zalecki, C. Garcia-Mateo, M. Opiela: Materials, 13, 2020, 958. https://doi.org/10.3390/ma13040958
38. C. Garcia-Mateo, T. Sourmail, A. Philippot, L. Morales-Rivas, J.A. Jimenez: Journal of Materials Research and Technology, 30, 2024, 6995-7005. https://doi.org/10.1016/j.jmrt.2024.05.090
39. Carl Andersson, Andreas Lundbäck: Metals, 16(7), 2026, 754. https://doi.org/10.3390/met16070754
40. A. Skowronek, A. Kozłowska: Journal of Thermal Analysis and Calorimetry, 150, 2025, 1069–1079. https://doi.org/10.1007/s10973-024-13662-y